

On the formation of hydrothermal vents and cold seeps in the Guaymas Basin, Gulf of California

Sonja Geilert¹, Christian Hensen¹, Mark Schmidt¹, Volker Liebetrau¹, Florian Scholz¹,
Mechthild Doll², Longhui Deng³, Annika Fiskal³, Mark A. Lever³, Chih-Chieh Su⁴, Stefan
Schlömer⁵, Sudipta Sarkar⁶, Volker Thiel⁷, Christian Berndt¹

¹GEOMAR Helmholtz Centre for Ocean Research Kiel, Wischhofstraße 1-3, 24148 Kiel, Germany

²Universität Bremen, Klagenfurter-Straße 4, 28359 Bremen, Germany

³Department of Environmental Systems Science, ETH Zurich, Universitätstrasse 16, 8092 Zurich, Switzerland

⁴Institute of Oceanography, National Taiwan University, No. 1, Sec. 4, Roosevelt Road, Taipei 106, Taiwan

⁵Federal Institute for Geosciences and Natural Resources, Stilleweg 2, 30655 Hannover, Germany

⁶Department of Earth and Climate Science, Indian Institute of Science Education and Research Pune, Dr. Homi Bhabha Road, Maharashtra-411008, India

⁷Geobiology, Geoscience Centre, Georg-August University Göttingen, Goldschmidtstr. 3, 37077 Göttingen, Germany

Abstract

The Guaymas Basin in the Gulf of California is an ideal location to investigate the hypothesis that magmatic intrusions into organic-rich sediments can cause the release of thermogenic methane and CO₂ which may contribute to climate warming. In this study pore fluids relatively close to a hydrothermal vent field and at cold seeps up to 30 km away from the northern rift axis were studied to determine the influence of magmatic intrusions on pore fluid composition and gas migration. Pore fluids close to the hydrothermal vent field show predominantly ambient diagenetic fluid composition, indicating a shallow circulation system transporting seawater to the hydrothermal catchment area rather than being influenced by hydrothermal fluids themselves. Only in the deeper part of the sediment core, composed of hydrothermal vent debris, ⁸⁷Sr/⁸⁶Sr ratios and slightly elevated Li concentrations indicate the minor admixture of hydrothermal fluids (~3%). Pore fluids at cold seeps also show a mainly ambient diagenetic fluid composition without any imprint from high temperature processes. Seep communities at the seafloor are mainly sustained by biogenic methane, which is rising along pre-formed pathways. Anaerobic oxidation of methane (AOM) is widespread at these sites as indicated by pore water profiles, isotope fractionation of hydrocarbons, as well as the occurrence of authigenic carbonates and indicative biomarkers.

Deep fluid and thermogenic gas flow might have been active during sill emplacement at the investigated sites, but ceased 28 to 7 kyears ago, based on sediment thickness above extinct conduits. Our results indicate that carbon release depends on the longevity of sill-induced hydrothermal systems, which is a currently unconstrained factor.

1 Introduction

Climate change events in Earth's history have been partly related to the injection of large amounts of greenhouse gases into the atmosphere (e.g. Svensen et al., 2004; Gutjahr et al., 2017). Among the most prominent of these events was the Paleocene-Eocene Thermal Maximum (PETM) during which the Earth's atmosphere warmed by about 8°C in less than 10,000 years (Zachos et al., 2003). The PETM was possibly triggered by the emission of about 2000 Gt of carbon (Dickens, 2003; Zachos et al., 2003). Processes discussed to release these large amounts of carbon in a relatively short time are gas hydrate dissociation and igneous intrusions into organic-rich sediments, triggering the release of carbon during contact metamorphism (Aarnes et al., 2010; Svensen et al., 2004). The Guaymas Basin in the Gulf of California is considered one of the few key sites to study carbon release in a rift basin exposed to high sedimentation rates.

The Gulf of California is located between the Mexican mainland and the Baja California Peninsula, north of the East Pacific Rise (EPR; Fig. 1). The spreading regime at EPR continues into the Gulf of California and changes from a mature, open ocean-type to an early-opening continental rifting environment with spreading rates of about 6 cm yr⁻¹ (Curry & Moore, 1982). The Guaymas Basin, which is about 240 km long, 60 km wide, and reaching water depths of up to 2000 m, is known as a region of vigorous hydrothermal activity (e.g. Curry and Moore, 1982; Gieskes et al., 1982; Von Damm et al., 1985). Its spreading axis consists of two graben systems (northern and southern troughs) offset by a transform fault (Fig. 1). In contrast to open ocean spreading centers like the EPR, the rifting environment in the Guaymas Basin shows a high sediment accumulation rate of up to 0.8-2.5 m kyr⁻¹ resulting in organic-rich sedimentary deposits of several hundreds of meters in thickness (e.g. Calvert, 1966; DeMaster, 1981; Berndt et al., 2016). The high sedimentation rate is caused by high biological productivity in the water column and influx of terrigenous matter from the Mexican mainland (Calvert, 1966).

Hydrothermal activity in the Guaymas Basin was first reported in the southern trough (e.g. Lupton, 1979; Gieskes et al., 1982; Campbell and Gieskes, 1984; Von Damm et al., 1985). Here, fluids emanate partly from Black Smoker type vents at temperatures of up to 315°C (Von Damm et al., 1985). Sills and dikes intruding into the sediment cover significantly affect temperature distribution and hence environmental conditions like early-diagenetic processes (Biddle et al., 2012; Einsele et al., 1980; Kastner, 1982; Kastner and Siever, 1983; Simoneit et al., 1992; Lizarralde et al., 2010; Teske et al., 2014). The heat released by magmatic intrusions accelerate early-diagenetic processes which strongly influence the chemistry of the interstitial waters (e.g. Gieskes et al., 1982; Brumsack and Gieskes, 1983; Kastner and Siever, 1983; Von Damm et al., 1985). Sills intruded into the sediment cover and cold seeps at the seafloor were observed up to 50 km away from the rift axis, and a recently active magmatic process triggering the alteration of organic-rich sediments and releasing thermogenic methane and CO₂ was proposed (Lizarralde et al., 2010). Varying methane concentrations and temperature anomalies in the water column may result from active thermogenic methane production generated by contact metamorphism (Lizarralde et al., 2010). This process might cause a maximum carbon flux of 240 kt C yr⁻¹ and might induce profound climatic changes.

During the SO241 expedition in June/ July 2015 a new hydrothermal vent field was discovered at the flank of the northern trough (Fig. 1; Berndt et al., 2016). The discovered mound rises up to 100 m above the seafloor and predominantly Black Smoker-type vents suggest similar endmember temperatures and geochemical composition as found at the southern trough (Von Damm et al., 1985; Von Damm, 1990; Berndt et al., 2016). The hydrothermal vent system emits methane-rich fluids with a helium isotope signature indicative of fluids in contact with mid-ocean ridge basalt. The vigorous release of large amounts of methane and CO₂ up to several hundred of meters into the water column led Berndt et al. (2016) to support the hypothesis that magmatic intrusions into deep sediments might have triggered the PETM during opening of the North Atlantic as proposed by Svensen et al. (2004).

During RV SO241 cruise SO241, we sampled the recently discovered hydrothermal vent in the northern trough (Berndt et al., 2016) and some of the off-axis seeps described by Lizarralde et al. (2010), which are located above potential sill intrusions. We collected sediment, carbonate, and water column samples. Here, we present fluid and/ or gas

geochemical data from the cold seeps, the hydrothermal vent field, the water column, and gas hydrates. In addition, an authigenic carbonate, exposed at the surface of one seep site, was examined. Furthermore, we performed seismic scans and temperature measurements. All data will be discussed in order to identify subsurface processes and fluid origin and will be compared to results by Lizarralde et al. (2010). Our data reveal that pore fluids and hydrocarbon gases at the seep locations essentially reflect shallow diagenetic processes. Hence, at the investigated sites (except close to the hydrothermal vent field), deep-seated, hydrothermal processes appear to be extinct nowadays suggesting that any sill-induced release of thermogenic methane highly depends on the longevity of the magmatic systems underneath.

2 Materials and methods

2.1 Sampling devices and strategy

During the RV SONNE expedition SO241 seven sites across the central graben of the Guaymas basin were investigated (Fig. 1). Site-specific sampling and data recording were performed using (1) a video-guided multicorer (MUC), (2) a gravity corer (GC), (3) temperature loggers attached to a GC or sediment probe, (5) a video-guided VCTD / Rosette water sampler, and (6) a video-guided hydraulic grab (VgHG). Sites were selected according to published data on the locations of seeps (Lizarralde et al., 2010) and seismic data acquired during the cruise (see below).

2.1.1 Seismic data recording

Seismic data were collected using a Geometrics GeoEel Streamer of 150 and 183.5 m length and 96 and 112 channels, respectively. Two generator-injector guns in harmonic mode (105/105 cubic inch) served as the seismic source. Processing included navigation processing (1.5625 m crooked line binning), 20, 45, 250, 400 Hz frequency filtering, and poststack Stolt migration with water velocity yielding approximately 2 m horizontal and 5 m vertical resolution close to the seafloor.

2.1.2 Sediment and pore fluid sampling

133

134 At seepage and vent sites, the video-guided MUC was used to discover recent fluid release,
135 which is indicated by typical chemosynthetic biological communities at the seafloor
136 (microbial mats, bivalves, etc.). However, small-scale, patchy distributions of active seepage
137 spots and visibility of authigenic carbonate concretions made it difficult to select the “best
138 possible” sampling locations for fine-grained sediment. Hence, comparing results from
139 different seeps might be biased in this regard as seepage areas might not have been the
140 the most active place. GC deployments were typically performed at presumed suspected MUC sites
141 or at the center of suspected seeps (based on bathymetry and seismic data).

142 In total, we present pore fluid and gas data collected at the seepage sites North (GC01,
143 MUC11), Central (GC03, GC13, GC15, MUC04), and Ring Seep (MUC05), one reference site
144 (see below; Reference Site; GC04, MUC02), and the hydrothermal vent field (Smoker Site;
145 GC09, GC10, MUC15, MUC16). The Reference Site, that did not show active seepage or faults
146 indicated by seismic data, was chosen to obtain geochemical background values. In addition,
147 the slope towards the Mexican mainland was sampled as well (Slope Site; GC07) (Fig. 1,
148 Table 1). Immediately after core retrieval, GCs were cut, split, and subsampled. Samples
149 were transferred into a cooling lab at 4°C and processed within 1 or 2 hours. Pore fluids were
150 obtained by pressure filtration (e.g. Jahnke et al., 1982). Sediment samples for hydrocarbon
151 gases were taken on deck with syringes and transferred to vials containing concentrated
152 NaCl solution (after Sommer et al., 2009). After MUC retrieval, bottom water was sampled
153 and immediately filtered for further analyses. The sediment was transferred into a cooling
154 lab and sampling was executed in an argon-flushed glove bag. Pore fluids were retrieved by
155 centrifugation and subsequent filtration using 0.2 µm cellulose acetate membrane filters
156 (e.g. Jahnke et al., 1982).

157

158 Figure 1: Sample locations in the Guaymas Basin, Gulf of California studied during RV SONNE
159 expedition SO241. (a) Overview of stations (Seep Sites, Smoker Site, and Slope Site). Black
160 square indicates enlargement area in (b). Site DSDP 477 in the southern trough is shown for
161 comparison. (b) Enlargement of the sampling locations. Red circles refer to GC employments
162 and yellow triangles to MUCs. Brown square at Graben Site refers to water column sampling
163 and temperature measurements. Black lines refer to seismic profiles, displayed in Fig. 2. (c)
164 Enlargement of Smoker Site sampling locations. Note the different scale compared to (a) and

(b). Black arrow refers to the location of the hydrothermal mound described in Berndt et al. (2016).

2.1.3 Subseafloor temperature measurements

Temperature gradients and thermal conductivity were measured at North Seep, Central Seep, Reference Site, and Smoker Site as well as along a transect across the newly discovered hydrothermal vent field and the rift valley (Graben Site). Miniaturized temperature loggers (MTL) were attached to GCs or to a 5 m long sediment lance at a sampling rate of 1 measurement per second. The absolute accuracy of these temperature measurements is about 0.1 K and the temperature resolution is 0.001 K (Pfender and Villinger, 2002).

Thermal conductivity was measured on recovered core material in close vicinity to the MTLs using the KD2 Pro Needle Probe instrument. For temperature measurements obtained by a lance, a constant thermal conductivity of $0.7 \text{ W m}^{-1} \text{ K}$ was assumed. Data processing was done according to Hartmann and Villinger (2002).

2.1.4 Water column sampling

Water samples were taken by using a video-guided Niskin Water sampler Rosette System (Schmidt et al., 2015) in order to study water column chemistry (i.e. dissolved CH_4) and oceanographic parameters (i.e. temperature, salinity, turbidity). Eight water sampling locations were chosen in the vicinity of MUC and GC stations and are termed North Seep (VCTD03), Central Seep (VCTD02), Ring Seep (VCTD01), Graben Site (CTD01; no video-guided sampling), Smoker Site (VCTD06 and 10), and Slope Site (VCTD07). Additionally, hydrocarbon data published in Berndt et al. (2016) from the hydrothermal plume (VCTD09) are shown. The (V)CTDs were either used in a towed mode (VCTD03, 06, 09, 10) or in station (CTD01; VCTD01, 02, 07) keeping hydrocast mode. The water depth was controlled based on pressure readings, altitude sensors (<50 m distance to bottom), and online video observation (1 - 2 m above the seafloor).

2.1.5 Authigenic carbonate sampling

At Central Seep a block (approx. 1 x 0.5 x 0.3 m) was recovered in 1843 m water depth from the surface of a typical cold seep environment (close to high abundance of tube worms) the deployment of a video-guided hydraulic grab (VgHG, GEOMAR). The block consisted mainly of solidified carbonate matrix covered by a whitish carbonate rim and was characterized by coarse open pore space in mm to cm scale (see supplementary Fig. S1).

2.2 Sample treatment and analytical procedures

Pore fluids were analyzed onboard for total dissolved sulfide (TH_2S) and NH_4 directly after recovery by photometer using standard methods described in Grasshoff et al. (2002). Prior to NH_4 measurements, pore fluids containing dissolved sulfide were treated with argon to prevent biased NH_4 measurements. Total alkalinity (TA) was determined by titration immediately after pore water separation using 0.02 M HCl (Ivanenkov and Lyakhin, 1978). Shore-based analyses of the remaining acidified pore water included dissolved anions (SO_4 , Cl) and cations (Li, Mg) using ion chromatography (IC, METROHM 761 Compact, conductivity mode) and inductively coupled plasma optical emission spectrometry (ICP-OES, VARIAN 720-ES), respectively. All chemical analyses were tested for accuracy and reproducibility using the IAPSO salinity standard (Gieskes et al., 1991).

Strontium isotope ratios were analyzed by Thermal Ionization Mass Spectrometry (TIMS, Triton, ThermoFisher Scientific). The samples were chemically separated via cation exchange chromatography using the SrSpec resin (Eichrom). The isotope ratios were normalized to the NIST SRM 987 value of 0.710248 (Howarth and McArthur, 2004) which reached a precision of ± 0.000015 (2 sd, $n = 12$). Potential influences of ^{87}Rb interferences on $^{87}\text{Sr}/^{86}\text{Sr}$ isotope ratios are eliminated by combining the highly selective Sr-Spec resin and Rb/Sr-discriminating TIMS pre-heating procedures with the static mode measurement of ^{85}Rb simultaneously to the Sr masses 84, 86, 87 and 88 for optional Rb/Sr corrections (not required in this study).

Water samples taken from Niskin bottles were transferred into 100 ml glass vials with helium headspace of 5 ml and poisoned with 50 μl of saturated mercury chloride solution.

228 Hydrocarbon composition of headspace gases was determined using a CE 8000 TOP gas
229 chromatograph equipped with a 30 m capillary column (Restek Q-PLOT, 0.32 mm) and a
230 flame ionization detector (FID). Replicate measurements yielded a precision of <3 % (2 sd).

231 Stable carbon isotopes of methane were measured using a continuous flow isotope ratio
232 mass spectrometer (cf-IRMS). A Thermo TRACE gas chromatograph was used to separate the
233 light hydrocarbon gases by injecting up to 1 ml headspace gas on a ShinCarbon ST100/120
234 packed gas chromatography column. The separated gases were combusted and
235 corresponding $\delta^{13}\text{C}$ values were determined using a Thermo MAT 253 mass spectrometer.
236 The reproducibility of $\delta^{13}\text{C}$ measurements was ± 0.3 ‰ (2 sd) based on repeated
237 measurements of the reference standard Vienna Pee Dee Belemnite (VPDB).

238 Stable hydrogen isotope compositions of methane were analyzed by separating methane
239 from other gases by online gas chromatography (Thermo Trace GC; isotherm at 30°C; 30 m
240 RT-Q-Bond column, 0.25 mm ID, film thickness 8 μm). Prior to stable isotope analysis using a
241 coupled MAT 253 mass spectrometer (Thermo) methane-H was reduced to dihydrogen at
242 1420°C. Data are reported in per mil relative to Standard Mean Ocean Water (SMOW). The
243 precision of $\delta\text{D-CH}_4$ measurements was ± 3 ‰ (2 sd).

244
245 ^{210}Pb (46.52 keV) and ^{214}Pb (351.99 keV) were simultaneously measured on freeze dried
246 sediments by two HPGe gamma spectrometry systems (ORTEC GMX-120265 and GWL-
247 100230), each interfaced to a digital gamma-ray spectrometer (DSPECPlus™). Efficiency
248 calibration of the gamma detectors were calibrated using IAEA reference materials, coupled
249 with an in-house secondary standard for various masses (Lee et al., 2004; Huh et al., 2006).
250 ^{214}Pb was used as an index of ^{226}Ra (supported ^{210}Pb) whose activity concentration was
251 subtracted from the total ^{210}Pb to obtain excess ^{210}Pb ($^{210}\text{Pb}_{\text{ex}}$). The activities of radionuclides
252 were decay-corrected to the date of sample collection. All radionuclide data are calculated
253 on salt-free dry weight basis.

254
255 A representative sample of the authigenic carbonate (cm-scale) was broken from the upper
256 surface of the block, gently cleaned from loosely bound sediment and organic remains and
257 dried at 20°C for 12 h. Two different subsamples were prepared by drilling material with a

handheld mm-sized mini-drill from the outer rim (whitish coating, lab code: 470-15) and the related inner core (dark matrix, lab code: 472-15).

Prior to aliquot procedures both subsamples were finely ground in an agate mortar providing homogeneous aliquots of suitable grain size for mineral identification by X-ray diffractometry (XRD) (Philips X-ray diffractometer PW 1710 in monochromatic CuK α mode between 2 and 70 2 θ (incident angle), for details see supplement). Subsamples were analyzed for $\delta^{18}\text{O}$ and $\delta^{13}\text{C}$ by stable isotope ratio mass spectrometry (SIRMS) and U-Th geochronology by multi collector-inductively coupled plasma-mass spectrometry (MC-ICP-MS) on a parallel leachate / sequential dissolution approach for single and isochron ages (method see supplement). Furthermore, $^{87}\text{Sr}/^{86}\text{Sr}$ isotope signatures for aliquots of the individual U-Th solutions by thermal ionization mass spectrometry (TIMS, for method details please refer to pore water Sr isotope analyses) were determined. Lipids extracts for biomarker termination were analyzed as well (see below).

From each homogenized carbonate powder sample (see above), an aliquot of 10 mg was separated for carbon $\delta^{13}\text{C}$ and oxygen $\delta^{18}\text{O}$ stable isotope analysis. A fraction from this (approximately 1 mg) was dissolved by water-free phosphoric acid at 73°C in a “Carbo-Kiel” (Thermo Fischer Scientific Inc.) online carbonate preparation line and measured for carbon and oxygen stable isotope ratios with a MAT 253 mass spectrometer (Thermo-Fischer Inc.). The $\delta^{13}\text{C}$ and $\delta^{18}\text{O}$ values are calculated as deviations from laboratory standard referred to the PDB scale and reported in ‰ relative to V-PDB. The external reproducibility was checked by replicate analyses of laboratory standards as being better than ± 0.04 ‰ for $\delta^{13}\text{C}$ and ± 0.1 ‰ for $\delta^{18}\text{O}$ (1 sd, n=7) for this sample set. However, the single measurement uncertainties were significantly better and the resulting 2 sd (n=3) for both main samples are given in the supplement Table S6.

Bioturbates were extracted from 4 g of powderized sample and were then sequentially extracted with dichloromethane (DCM)/methanol (3/1, v/v), DCM, and *n*-hexane (ultrasonication, 20 min). The combined extracts were dried, derivatized using a BSTFA/trimethylchlorosilane mixture (95/5, v/v; 1h; 40°C) and analysed by coupled gas chromatography-mass spectrometry (GC-MS). GC-MS analyses were carried out with a Thermo Fisher Trace 1310 GC coupled to a Quantum XLS Ultra MS. The instrument was equipped with a Phenomenex Zebron ZB 5MS capillary column (30 m, 0.1 µm film thickness, inner diameter 0.25 mm). Fractions were injected splitless at 270°C. The carrier gas was He (1.5 mL/min). The GC oven temperature was ramped from 80°C (1 min) to 310°C at 5°C min⁻¹ and held for 20 min. Electron ionization mass spectra were recorded at 70 eV.

3 Results

3.1 Subsurface structure and evidence for sill-related fluid mobilization

Seismic profiles show a wide range of sediment deformation (Fig. 2). Seismic amplitude blanking along vertical zones below the seafloor indicates the flow of gaseous pore fluids at North, Central, and Ring Seep (Fig. 2). Underneath these locations sediments are deformed, probably due to sediment mobilization associated with hydrothermal activity in response to sill intrusion. In contrast the Reference Site sediments show a more or less continuous succession without vertical disturbance. At North Seep, a shallow high-amplitude reversed polarity reflector occurs at 50-60 ms. Sill depths are inferred from the seismic profiles at ~500 to 600 meter below seafloor (mbsf) for North Seep and with ~350 to 400 mbsf at the other sites, assuming seismic interval velocities of 1600 to 2000 m s⁻¹. Seismic images suggest that massive disturbance of sediments and vertical pipe structures are related to channeled fluid and/or gas advection caused by sill intrusions (Fig. 2). Faults are indicated which may serve as fluid pathways above potential sill intrusions. Closer inspection of the seismic reflectors at the Central Seep (Fig. 2c) shows onlap onto a doming structure. On the NW flank of the dome the deepest onlap occurs at 60 ms or 48 mbsf (assuming 1600 m s⁻¹ sediment interval velocity) whereas on the SE flank the shallowest onlap occurs at 15 ms or 12 mbsf.

Figure 2: Seismic profiles of North Seep (a), Smoker Site (b) as well as of Central Seep and Reference Site (c). Seismic section showing doming above the Central Seep. There are different phases of onlap starting about 60 ms (maximum deposition) until about 15 ms (minimum deposition) or 48 and 12 mbsf respectively assuming a sediment interval velocity of 1600 m s^{-1} .

3.2 Temperature measurements

Heat flow and temperature gradients were measured at North and Central Seep, Reference Site, and Smoker Site (attached to GCs) as well as in transects along the hydrothermal ridge and rift axis (attached to a temperature lance; Fig. 3 and S2, Table 1). Temperature gradients are shown in Figure S2. Highest heat flows occurred close to the Smoker Site and ranged between 599 and 10835 mW m^{-2} . Temperature gradients were also highest at the Smoker Site ($\sim 15 \text{ K m}^{-1}$). In contrast, heat flows and temperature gradients in the rift valley close to the rift axis ranged between 262 and 338 mW m^{-2} and 0.4 to 0.5 K m^{-1} , respectively. Generally heat flow values decreased with increasing distance to the rift axis with 140 mW m^{-2} at the Reference Site, 113 mW m^{-2} at Central Seep, and 28 mW m^{-2} at North Seep. Temperature gradients are 0.22 K m^{-1} at the Reference Site, 0.16 K m^{-1} at Central Site and 0.14 K m^{-1} at North Site.

Figure 3: (a) Heat flow in the vicinity of the northern trough. Note the different heat flow scale in the enlarged area of the Smoker Site (b).


3.3 Sediment characteristics and sedimentation rates

The sediments are mainly composed of organic-rich diatomaceous clay, consistent with earlier analyses (e.g. Kastner, 1982). At North Seep, the sediments are composed of homogeneous diatomaceous clay containing rare shell fragments and carbonate concretions. Gas hydrates were discovered at 2.5 mbsf. Authigenic carbonates were exposed at the seafloor. At Ring Seep, SW of North Seep, sediments are predominantly composed of diatomaceous clay. At Central Seep, located between North Seep and Smoker Site, sediments are composed of homogeneous diatomaceous clay intercalated with whitish

layers and shell fragments occurring shallow in the sediment ($\leq 70\text{cm}$). Again, authigenic carbonates were observed on the seafloor. At Smoker Site, ca. 500 m SE of the hydrothermal vent field, surface sediments are likewise composed of diatomaceous clay with light and dark greyish banding. Traces of bioturbation are visible in the upper 4 m. At this depth, a sharp contact defines the transition to the underlying hydrothermal deposits, which are composed of mm-to-cm sized black to grey Fe-rich sulfides (for a detailed description see Berndt et al. (2016)). Within the hydrothermal deposits brownish to grey clay lenses appear. At the Slope Site, sediments are laminated in the mm- to cm-range. The sediment is dominated by diatomaceous clay that contains a few ash lenses. The sedimentation rates ranged between 0.4 m kyr^{-1} at Smoker Site and 3.5 m kyr^{-1} at North Seep based on radionuclide measurements (Table 1). Sedimentation rates at all other sites are about 2 m kyr^{-1} .

3.4 Pore water geochemistry

All pore water data and isotope measurements of $^{87}\text{Sr}/^{86}\text{Sr}$ are listed in supplementary Tables S1 and S2. Pore water profiles of TA, TH_2S , SO_4 , CH_4 , NH_4 , Cl, Mg, and Li are shown in Fig. 4a (GCs) and 4b (MUCs).

 Figure 4: Pore water profiles of GCs (a) and MUCs (b). For Central Seep, GC13 is shown exemplary here, geochemical data of the remaining cores (GC03, 15) can be found in Table S1. Endmember composition of hydrothermal solutions from Von Damm et al. (1985) and hydrothermal plume geochemical composition from Berndt et al. (2016) are shown in (a) for comparison.

Pore water constituents plotted in Figure 4 were selected to characterize variations in organic matter diagenesis, anaerobic oxidation of methane (AOM), as well as potential water-rock interactions related to subsurface hydrothermal activity. In general, methane concentrations are elevated at the seep locations and at the slope, thus enhancing AOM. TA and TH_2S increase with depth for North Seep, Central Seep (only MUC04), and Slope Site, while SO_4 is decreasing. AOM depths can only be inferred for North Seep with $\sim 160\text{ cm}$ and Slope Site with $\sim 300\text{ cm}$. NH_4 is only slightly increasing with depth; higher NH_4 -levels are only

found at the Slope Site (Fig. 4). Concentrations of Cl, Mg, and Li do not show significant variations from seawater in shallow sediment depths (MUCs). At greater depths (GCs) some deviations from seawater concentration occur at North Seep, Smoker Site, and Slope Site. At North Seep, Mg shows a minor offset at ~150 cm depth, while at Smoker Site Mg concentrations increase continuously. In GC09 at Smoker Site, Li concentrations increase and Mg concentrations decrease abruptly in a depth of ~400 cm. At the Slope Site, Mg increases slightly below 400 cm sediment depth while Li shows a small decrease above 400 cm. Sr concentrations and isotopes are plotted in Fig. 5. Sr concentrations show predominantly modern seawater values, except at North Seep where they strongly decrease. The $^{87}\text{Sr}/^{86}\text{Sr}$ isotope ratios also show predominantly seawater values (0.709176; Howarth and McArthur, 2004), except for the Smoker Site where the isotope ratios decrease strongly below the transition between hemipelagic sediments and hydrothermal deposits (Fig. 5). North and Ring Seeps as well as Smoker Site (GC10) show slight decreases in $^{87}\text{Sr}/^{86}\text{Sr}$. The ratios show a similar depletion as those from the hydrothermal plume (Berndt et al., 2016).

Figure 5. Sr concentrations and $^{87}\text{Sr}/^{86}\text{Sr}$ ratios for GCs (a) and MUCs (b). For comparison, data from the hydrothermal plume (Berndt et al., 2016), the hydrothermal endmember (Von Damm et al., 1985), and modern seawater (Howarth and McArthur, 2004) are shown. Note the different x-axis scales for MUC Sr concentration and $^{87}\text{Sr}/^{86}\text{Sr}$ ratios.

3.5 Hydrocarbon gases, carbon and hydrogen isotope data

Concentrations of dissolved hydrocarbons and $\delta^{13}\text{C}_{\text{CH}_4}$, $\delta^{13}\text{C}_{\text{C}_2\text{H}_6}$, and $\delta\text{D}_{\text{CH}_4}$ data are reported in supplementary Table S3. Overall, our pore fluid data show a large variability in $\text{CH}_4/(\text{C}_2\text{H}_6+\text{C}_3\text{H}_8)$ with ratios between 100 and 10,000 and $\delta^{13}\text{C}_{\text{CH}_4}$ between -26.5 and -88.2 ‰. Gas hydrate $\delta^{13}\text{C}_{\text{CH}_4}$ ranges between -57.9 and -58.9 ‰. The $\delta^{13}\text{C}_{\text{C}_2\text{H}_6}$ values range between -26.1 and -38.3 ‰ for North Seep and -29.6 and -37.7 ‰ for Central Seep. The $\delta\text{D}_{\text{CH}_4}$ values at both seeps range between -97 and -196 ‰, for the gas hydrates between -196 and -198 ‰, for Slope Site between -192 and -196 ‰, and for the hydrothermal plume between -98 and -113 ‰ (VCTD09).

3.6 Water column data

Water column characteristics like temperature, salinity, turbidity, and methane concentrations are shown in Fig. 6 and Table S4. Surface waters in the Guaymas Basin show warm temperatures up to 29.5°C (salinity: 34.5 ‰) close to the Mexican mainland (Slope Site, VCTD07) and up to 24.6°C (salinity: 34.6 ‰) in the central basin (Central Seep, VCTD02). With depth, temperatures decrease continuously and range between 2.8 and 3.0°C (salinity: 34.6 ‰) close to the sea floor (1600 – 1800 m). Turbidity values are high in the deep water layer (~1400-1800 m) and indicate a well-mixed deep basin, also shown by relatively homogeneous temperature and salinity data. Only the water column directly above the hydrothermal vent field shows strongly elevated temperature (28.4°C) and salinity (35.1 ‰) (Berndt et al., 2016). Methane concentrations are highest close to the hydrothermal vent field (up to 400 µM, (VCTD09, Berndt et al., 2016), but still vary in the deep water column of the basin between 2 and 28.1 nM (Central Seep (VCTD02) and Ring Seep (VCTD01), respectively).

Figure 6: Water column temperature, salinity, turbidity, and methane concentrations. Note that the upper ~300 m below sea level (bsl) in the turbidity data are not shown for scale matters. VCDT09 and temperature data from VCDT10 are from Berndt et al. (2016), all other parameters were acquired in this study.

3.7 Authigenic carbonate data

The authigenic carbonate sample (Fig. S1) consists of 88 to 90 % aragonite and 6 to 12 % calcite (supplementary Table S5). By the uncertainty related maximum deviation of Δd_{104} (< 0.01) the XRD spectrum identifies calcite with a Mg fraction below 3 % according to Goldsmith et al. (1961). The bulk outer rim carbonate has an average carbon isotope signature ($\delta^{13}\text{C}_{\text{V-PDB}}$) of -46.6 ± 0.2 ‰ and an oxygen isotope signature ($\delta^{18}\text{O}_{\text{V-PDB}}$) of 3.7 ± 0.3 ‰. Inner core carbonate isotope signatures yield similar values with $\delta^{13}\text{C}_{\text{V-PDB}}$ of -44.7 ± 0.4 ‰ and $\delta^{18}\text{O}_{\text{V-PDB}}$ of 3.6 ± 0.1 ‰ (Table S5). The average outer rim $^{87}\text{Sr}/^{86}\text{Sr}$ ratio is 0.709184 ± 0.000027 and the inner core ratio is 0.709176 ± 0.000003 . The U-Th carbonate dating approach on these authigenic carbonates implies formation ages younger than 240 yrs BP.

Lipid extracts obtained from seep carbonate 56-VgHG-4 (Central Seep) revealed a strong signal of specific prokaryote-derived biomarkers (Fig. S1). These compounds encompassed isoprenoid lipids derived from archaea namely crocetane, 2,6,10,15,19-pentamethylicosane(-icosenes (PMI, PMI Δ) archaeol, and *sn*2-hydroxyarchaeol (see Fig. S1 for structures). In addition, the sample contained a suite of non-isoprenoid 1,2-dialkylglycerolethers (DAGE) of bacterial origin. Typical compounds of planktonic origin, such as sterols, were also present, but low in abundance.

4 Discussion

4.1 Origin of seeping fluids

4.1.1 Smoker Site

The water column above the newly discovered hydrothermal vent field exhibits elevated CH₄ concentrations (up to 400 μ M) and pCO₂ data (>6000 μ atm) (Berndt et al., 2016). The range of the measured stable isotope signature of methane ($\delta^{13}\text{C}_{\text{CH}_4}$ between -39‰ and -14.9‰) and the helium isotope anomaly (³He/⁴He ratio of 10.8×10^{-6}) clearly indicate gas exhalations from thermogenic organic matter degradation with contributions from a mantle source (see Berndt et al., 2016). These northern trough hydrothermal fluids are comparable in their gas geochemistry to the southern trough (Lupton, 1979; Von Damm et al., 1985; Berndt et al., 2016). However, the highest heat flow values of up to 10835 mW m⁻² measured in this study are found close to the Smoker Site and are much higher than those observed in earlier studies (maximal 2000 mW m⁻², Fisher and Becker, 1991). The high heat flow at Smoker Site even exceeds the hydrothermally more active southern trough where heat flow values of 2000 to 9000 mW m⁻² were measured (Lonsdale and Becker, 1985; Fisher and Becker, 1991). This might indicate that hydrothermal activity at the northern trough is younger and possibly a more recent process compared to the southern trough.

Hydrothermal fluids are typically depleted in Mg and highly enriched in fluid-mobile elements like Li caused by high-temperature reactions with mafic rocks (here sills) and/ or sediments through which they percolate (e.g. Einsele et al., 1980; Gieskes et al., 1982; Kastner, 1982; Von Damm et al., 1985; Lizarralde et al., 2010; Teske et al., 2016). Such compositions were reported from DSDP site 477 (Gieskes et al., 1982) and fluids obtained by Alvin dives (Von Damm et al., 1985) (see Fig. 1 for location of Site DSDP 477). Although

strongly diluted, CTD samples from the hydrothermal plume in the northern trough show this trend (Berndt et al., 2016).

An indication for the presence of hydrothermal fluids in pore waters in the vicinity of the hydrothermal vent field is found at about 4 m depth in core GC09. Here, positive Li and negative Mg concentrations (Fig. 4a) are probably caused by weak admixing of hydrothermal solutions (Gieskes et al., 1982; Hensen et al., 2007). Likewise, $^{87}\text{Sr}/^{86}\text{Sr}$ isotope ratios decrease to a value of 0.708949 (Fig. 5) and thus tend towards the $^{87}\text{Sr}/^{86}\text{Sr}$ ratio of the local hydrothermal endmember ($^{87}\text{Sr}/^{86}\text{Sr} = 0.7052$; Von Damm, 1990). Hydrothermal endmember Li concentrations in the Guaymas Basin have been reported in a range between 630 and 1076 μM (Von Damm et al., 1985) and are 20 to 30 times higher than those measured at Smoker Site ($\sim 34 \mu\text{M}$; Fig. 4a, Table S1). Here, hydrothermal fluids account for about 3 % in the mix with seawater (Fig. 7). The sediments in this core section also change from diatomaceous clay to unconsolidated, coarse-grained hydrothermal deposits (Fe-rich sulfides; see also Sect. 3.3) which may facilitate the circulation of hydrothermal fluids.

Despite the proximity of the remaining GCs and MUCs to the hydrothermal vent field (~ 500 m distance; temperatures immediately after retrieval are up to 60°C) typical pore fluid indicators such as Mg, Li, and $^{87}\text{Sr}/^{86}\text{Sr}$ do not show major excursions from seawater values (Fig. 4). Similarly, NH_4 , an indicator for a diagenetic or catagenetic breakdown of organic matter, is only poorly enriched in sediments surrounding the hydrothermal vents ($\text{NH}_4 \leq 0.3$ mM). NH_4 remains well below the value reported from the southern trough (20 mM; Von Damm et al. (1985)) and the Slope Site (GC07) where 10 mM are reached already at subsurface depths of only a few meters (Fig. 4). The pore fluid geochemistry around the hydrothermal vent field therefore confirms that early-diagenetic processes are not intense (Fig. 7) and that the shallow sediments are not significantly affected by hydrothermal fluids. We hypothesize that hydrothermal venting causes a shallow convection cell drawing seawater through the sediments towards the hydrothermal vent field, while the sediments become heated by lateral heat conduction (cf. Gamo et al., 1991; Henry et al., 1996; Kinoshita and Yamano, 1997).

Fig. 7: NH_4 (μM) versus Li concentrations (μM) of Guaymas Basin cold seeps (North, Central) and the Smoker Site. Deep fluids from Smoker Site (GC09) mix with hydrothermal fluids with a share of $\sim 3\%$. The mixing line has been calculated following: $x_{\text{mix}} = x_{\text{phase1}} * f_1 +$

$x_{phase2} * f_2$ (1), with $f_1 + f_2 = 1$. Endmember 1 is the Guaymas Vent South (Von Damm, 1985, 1990) and endmember 2 is Guaymas North Seep. For comparison, Guaymas hydrothermal endmember fluid composition (Von Damm, 1985, 1990), hydrothermal plume fluid composition (Berndt et al., 2016), Guaymas slope sediments (GC07), and deep-sourced cold seeps (Aloisi et al., 2004; Hensen et al., 2007) are shown.

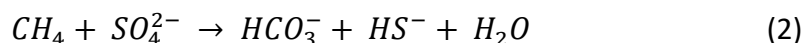
The diatomaceous clay might act as a seal to upwards migrating fluids, which are channeled to the catchment area of the rising hydrothermal fluids of the hydrothermal vent field (see also Berndt et al., 2016, their Fig. 4). The geochemical composition of these fluids is likely influenced by high temperature chemical alteration of the sediment caused by the intruded sills (Fig. 2b). However, shallower pore fluids of surface sediments at the Smoker Site (i.e. 0-4 m) are not much affected by contributions from these fluids and show predominantly ambient diagenetic fluid signatures.

4.1.2 Cold seeps

The selection of sampling sites at presumed seep locations was based on existing published data (Lizarralde et al., 2010) and information from seismic records (Fig. 2). Seismic amplitude blanking along vertical zones below the seafloor indicates active fluid and/ or gas conduits at North and Central Seep. Given that sill intrusions and related high-temperature alteration of sediments are driving the seepage, the expectation was to find deeply-sourced (average sill depth ~400 m) fluids with a typical geochemical signature analogous to findings at hydrothermal vents in the Guaymas Basin (Von Damm et al., 1985; Von Damm, 1990; Berndt et al., 2016). Such characteristics are e.g. a high concentration of thermogenic hydrocarbon gases formed by organic-matter degradation, enrichments in NH_4 , depletion in Mg, and a strong enrichment in fluid-mobile tracers like Li and B (e.g. Aloisi et al., 2004; Scholz et al., 2009). Hydrocarbon formation caused by abiogenic processes plays only a minor role in the hydrothermal vent field (McDermott et al., 2015; and discussion in Berndt et al. (2016)).

Samples obtained using a video-guided MUC revealed the highest methane concentrations at North, Central, and Ring Seeps (Fig. 4b). In conjunction with visual evidence (abundant chemosynthetic biological communities) this confirms that we have hit active seepage areas

during our sampling campaign. At the two most active sites, North and Central, high methane levels are accompanied by a significant drop in sulfate and increase in TA and TH₂S, providing evidence for AOM, according to the net reaction:



(e.g. Nauhaus et al., 2005; see Wegener et al., 2016 for a recent update).

These pore water trends are even more pronounced in GC01 (North) where the AOM zone was completely penetrated and gas hydrate was found at about 2.5 mbsf. Unfortunately, GCs from similarly active sites could not be obtained from Central and Ring Seeps, mainly because of patchiness of seepage spots and widespread authigenic mineralizations at the seafloor preventing sufficient penetration. Nevertheless, active methane seepage at all three investigated sites is evident. The methane flux is, however, not accompanied by any significant excursion of pore water constituents typical for deeply-sourced, high-temperature sediment-water interactions (e.g. Mg, Cl, Li). Also Sr concentrations show seawater values at all seep sites (Fig. 5), except for North Seep where values drop together with Ca due to co-precipitation during carbonate formation. The ⁸⁷Sr/⁸⁶Sr ratios show predominantly seawater signatures as well (Fig. 5, Table S2). Similarly, low NH₄ concentrations of <1 mM indicate a low intensity of organic matter decomposition (as discussed in Sect. 4.1.1). Taken together, our data show that, with exception of methane and sulfate, the pore water corresponds to ambient diagenetic conditions that are typically met in this shallow subsurface depth. An explanation for the decoupling of methane levels and pore water composition is that only methane is rising to the seafloor as a free gas. This assumption requires a closer look at the composition of dissolved hydrocarbons in general, which is given below.

4.2 Origin of hydrocarbon gases

4.2.1 Alteration effects

The origin of hydrocarbon gases can be deciphered by plotting CH₄/(C₂H₆+C₃H₈) ratios versus δ¹³C_{CH4} data in a modified Bernard diagram (Schmidt et al., 2005 and literature therein) (Fig. 8a) and δ¹³C_{CH4} versus δD_{CH4} after Whiticar (1999) and Welhan (1988) (Fig. 8b). Most of the

measured stable isotope data of pore water methane indicate a microbial origin or a mixed microbial and thermogenic origin (Fig. 8). By contrast, hydrocarbons venting at the hydrothermal vent field reflect a mixture of thermogenic methane and abiogenic methane derived from water-rock interactions (Berndt et al., 2016).

Figure 8: Hydrocarbon, $\delta^{13}\text{C}_{\text{CH}_4}$ and δD isotope data for Guaymas Basin seep sites, Smoker and Slope Site. Hydrothermal plume data are shown for comparison. Note that hydrocarbon and $\delta^{13}\text{C}_{\text{CH}_4}$ data are from Berndt et al. (2016). (a) $\text{CH}_4/(\text{C}_2\text{H}_6+\text{C}_3\text{H}_8)$ ratios versus $\delta^{13}\text{C}_{\text{CH}_4}$ data are shown after a modified Bernard diagram (Schmidt et al., 2005). Pale symbols indicate samples above the AOM zone. Rayleigh fractionation lines show the effect of (microbial) methane oxidation, labels indicate the residual methane in %. (b) Carbon ($\delta^{13}\text{C}_{\text{CH}_4}$) and hydrogen ($\delta\text{D}_{\text{CH}_4}$) isotope data after Whiticar (1999) and (Welhan, 1988). Pale symbols (Central Seep (MUC04)) indicate samples above AOM zone.

Interestingly, all but three North Seep sediments, analyzed for $\delta^{13}\text{C}_{\text{CH}_4}$ are located above the AOM zone (see Fig. 4) and could therefore be affected by microbial metabolisms utilizing electron-acceptors other than sulfate, namely nitrate, manganese(IV) or iron(III) (e.g. Jørgensen, 1996). AOM enriches DIC in ^{12}C and results in progressively increasing $\delta^{13}\text{C}_{\text{CH}_4}$ values in the residual methane (Whiticar, 1999). Considering the $\delta^{13}\text{C}_{\text{CH}_4}$ at Slope Site as a microbial endmember composition for the Guaymas Basin (Fig. 8a), most of the data fall on calculated fractionation lines for AOM following a Rayleigh trend (Whiticar, 1999). Methane sampled close to the Smoker Site (MUC15) is obviously also affected by AOM (Fig. 8a). This is in line with recent studies on hydrothermal sediments of the southern trough of the Guaymas Basin, where bacterial and archaeal communities catalyze the oxidation of methane and higher hydrocarbons and shift $\delta^{13}\text{C}_{\text{CH}_4}$ values to heavier signatures (Dowell et al., 2016).

The origin of methane and oxidation effects can further be identified in the $\delta^{13}\text{C}_{\text{CH}_4}$ versus $\delta\text{D}_{\text{CH}_4}$ plot after Whiticar (1999) and Welhan (1988) (Fig. 8b). Slope Site samples plot in the field of microbial CO_2 reduction while hydrothermal plume samples plot in the thermogenic field. One sample even points to a mantle signature, and thus shows potential endmember isotope signatures (Berndt et al., 2016). North Seep samples (pore fluids and gas hydrates)

plot in the mixing region while samples from Central Seep clearly shift away from the microbial field and are considered to be affected by bacterial oxidation (Whiticar, 1999).

Considering the methane below the AOM as being unaltered, three North Seep samples and the majority of the Slope Site samples show a clear microbial source of methane (Fig. 8a). All other samples appear to be affected by major oxidation following a Rayleigh fractionation process and show that only a fraction between 2 % (MUC04, Central Seep) and 0.05 % (GC15, Central Seep) remains as unoxidized methane (Fig. 8a).

4.2.2 Origin of unaltered samples

The $\delta^{13}\text{C}_{\text{CH}_4}$ versus $\delta\text{D}_{\text{CH}_4}$ plot of unaltered North Seep samples suggests a mixing of microbial and thermogenic methane (Fig. 8b). Similar signals have also been observed at Hydrate Ridge (Milkov et al., 2005) and seem to be a common phenomenon in hydrothermal and cold seep affected sediments. In a few samples from North and Central Seep ethane concentrations have been high enough to measure stable carbon isotopes and the $\delta^{13}\text{C}_{\text{C}_2\text{H}_6}$ values point to a thermogenic origin (Table S3).

4.3 Timing of active (thermogenic) methane release

4.3.1 Seep site geochemistry

Based on our data set no deep-sourced fluid is currently migrating upwards at the cold seeps investigated (compare deep-sourced seepage sites from the Gulf of Cadiz in Fig. 7). Hence, in terms of the original hypothesis that fluid emanation is directly linked to recent sill intrusions, these cold seep sites cannot be considered as being active as claimed by Lizarralde et al. (2010). These authors argued that thermogenic carbon is currently released up to 50 km away from the rift axis causing a maximum carbon flux of 240 kt C yr^{-1} . Further, Lizarralde et al. (2010) showed temperature anomalies, high methane concentrations, and helium isotopic anomalies in the water column potentially indicative of a magmatic source. These anomalies were detected in close vicinity to bacterial mats, tubeworms, and authigenic carbonates, situated above areas of sill intrusions. Comparable structures have been identified in this study by video-guided MUCs and seismic data (Fig. 2). Our detailed results on pore fluid, water column, and gas geochemistry now show that most methane

was of microbial origin (Fig. 8) and only traces of thermogenic methane were found up to ~20 km off axis (North Seep). Even pore fluids taken close to the hydrothermal vent field are dominated by shallow microbial degradation processes, indicating that hydrothermal fluid flow in the Guaymas Basin is rather localized and bound to focused fluid pathways. The temperature and chemical anomalies detected by Lizarralde et al. (2010) might also arise from the deep water layer in the Guaymas Basin itself which is influenced by hydrothermal fluids (Campbell and Gieskes, 1984). Hydrothermal activity in the Guaymas Basin produces hydrothermal plumes which are rising 100-300 m above seafloor and spreading out along density gradients throughout the basin (Campbell and Gieskes, 1984). Our results nevertheless show that the Guaymas Basin has a well-mixed bottom seawater layer with temperatures ranging between 2.8 and 3.9°C in >1000 m depth and off-axis methane concentrations that vary quite considerably (e.g. 6 to 28 nM at Ring Seep, Fig. 9). These bottom seawater variabilities are bigger than the reported anomalies by Lizarralde et al. (2010) and might indicate that thermogenic methane release might not be as widespread as suspected before.

Figure 9. Water column CH₄ (a) and temperature (b) at cold seeps as well as Smoker and Graben Site relative to the rift axis.

Pore fluids taken in a transect up to ~30 km away from the rift axis show no evidence for high-T reactions (Fig. 4, 7). We can still not exclude the possibility that thermogenic methane is released in other areas of the basin, but the lack of evidence for high temperature geochemical processes at our sites is evident and clearly contradicts with the conclusions drawn by Lizarralde et al. (2010). Our findings suggest that a projection of the thermogenic methane release based on the number of detected sills (Lizarralde et al., 2010) represents a maximum estimate as it does neither consider the time of the emplacement of a sill nor the lifetime of such magmatic systems. Today, shallow microbial degradation processes determine pore fluid signatures (Fig. 4, 8). Whereas high temperature thermogenic reactions have certainly been active during sill emplacement and once released large amounts of carbon, these processes have apparently ceased. However, pipe structures may still act as high-permeability pathways and facilitate the advection of gas. As a result, small amounts of thermogenic carbon might be released as reflected by the signatures of $\delta^{13}\text{C}_{\text{CH}_4}$ and

thermogenic $\delta^{13}\text{C}_{\text{C}_2\text{H}_6}$ isotope data at North and Central Seep. However, present methane advection rates are slow (probably $<1 \text{ cm yr}^{-1}$) as observed by low methane gradients in the pore fluid profiles (Fig. 4). These conditions favor an effective turnover of CH_4 to bicarbonate and authigenic carbonates by AOM (Wallmann et al., 2006; Karaca et al., 2010).

4.3.2 Origin of the authigenic carbonate

The porous authigenic carbonate block recovered from the seafloor at Central Seep can preserve long-term information about seepage in this area. The predominant biomarkers found in the seep carbonate from the Central Site (56-VgHG-4) are consistent with microbial consortia performing AOM. In particular, high abundances of crocetane and *sn*2-hydroxyarchaeol indicate major contributions from methanotrophic archaea of the ANME-2 cluster, whereas DAGE originate from syntrophic sulfate-reducing bacteria, probably of the *Desulfosarcina–Desulfococcus* group (Blumenberg et al., 2004; Niemann and Elvert, 2008). These consortia gain energy from AOM with sulfate as the final electron acceptor (see Eq. (2)).

At Central Seep, the increase in TA due to the AOM reaction plausibly explains the precipitation of isotopically depleted authigenic carbonates. Particularly, ANME-2 biomarkers have been reported in association with abundant fibrous, often botryoidal aragonite cements (Leefmann et al., 2008), which is in line with the observations made at the Central Seep (see Sect. 3.3). Moreover, the high abundance of ANME-2 indicates that seep carbonate formation took place under high sulfate concentrations, strong advective methane flow, but no elevated water temperatures (c.f. Nauhaus et al., 2005; Peckmann et al., 2009; Timmers et al., 2015). Minor amounts of typical marine sterols also show that the seep carbonates also captured detritus from the surrounding sediment and water column during their ongoing cementation.

The bulk carbonate carbon isotope signature ($\delta^{13}\text{C}_{\text{V-PDB}} = -46.6\text{‰}$) overlaps with the shallow heavy $\delta^{13}\text{C}_{\text{CH}_4}$ values (-27.5 and -48.6 ‰) in the pore fluids at Central Seep and confirms a dominant AOM signature with a minor planktonic and potentially $\delta^{13}\text{C}$ diluting background signal. The oxygen isotopes point to a low formation temperature of about 3°C , consistent with a precipitation in bottom waters (2.8 to 3.0°C (Fig. 6, 9; Table S4). The $^{87}\text{Sr}/^{86}\text{Sr}$ analyses support this assumption by values within uncertainty identical to modern seawater. U-Th

carbonate dating provide ages younger than 240 yrs BP. Summarizing, authigenic carbonates originate from shallow methane and were sub-recently formed in ambient seawater.

4.3.3 Timing of off-axis hydrothermal activity

The seismic data taken across the seep locations indicate that the disrupted sediment layers are not reaching to the sediment surface (Fig. 2a, c). This implies that fluid mobilization ceased at some time before the uppermost sediment layers were deposited. The doming above the Central Seep provides some clues on the timing of fluid migration (Fig. 2c). Assuming that the doming is the result of buoyancy-related uplift (Koch et al., 2015) it represents the time when intrusion-related gas reached the sea floor. Assuming further a sedimentation rate of 1.7 m per 1000 years (Central Seep; Table 1) and maxima and minima deposition depths of 48 and 12 m below seafloor, respectively (see Fig. 2c) this would imply that most of the gas reached the seafloor between 28 and 7 kyrs ago. Even at maxima and minima sedimentation rates of 3.5 m (North Seep) and 0.5 m (Ring Seep) per 1000 years, gas flow would have ceased between 14 and 3 kyrs ago at the earliest and between 96 and 24 kyrs ago at the latest. Accordingly, this finding further supports the results of the pore fluid and gas geochemistry which show no sign of active fluid flow from depth at the cold seep sites in the northern Guaymas Basin.

We agree with Lizarralde et al. (2010) that hydrothermal activity in the Guaymas Basin is an important driver for CH₄ (and CO₂) emissions into bottom waters. However, our data set shows that there is no deep fluid advection at the investigated sites. Our interpretation is that hydrothermal activity at these off-axis locations has ceased and previously formed pathways seem to mediate the advection of biogenic gas at present. It is not unlikely that seep-induced, hydrothermal activity is still ongoing in other places than those investigated in this study, but in order to provide more accurate predictions for (thermogenic) carbon fluxes and the potential impact on climate, sill emplacement mechanisms need to be better constrained. Apart from their spatial distribution, the most important and currently unknown factors are the determination of the time of their emplacement and the longevity of the sill-systems that require further investigation.

5 Conclusions

Magmatic intrusions into organic-rich sediments can potentially release large amounts of carbon into the water column and atmosphere and are therefore discussed as potential trigger mechanisms for rapid climate change, e.g. during the PETM. In the Guaymas Basin, off-axis cold seeps do not show indications for present-day hydrothermal activity. Pore fluids sampled from cold seeps and in the vicinity of hydrothermal vents in the northern Guaymas Basin are dominated by ambient diagenetic composition and show no sign of deep fluids or temperature-related diagenesis. Methane at the investigated sites shows a mixed origin (biogenic and thermogenic), with a main contribution from microbial processes. We suggest that hydrothermal circulation has largely stopped at depth and, based on seismic data, ceased more than 7 kyrs ago. Likewise, authigenic carbonates formed at cold seeps originate from shallow methane and were sub-recently formed in ambient seawater. Sill-induced hydrothermal systems appear to be an effective way to release carbon, but the longevity of this type of magmatic systems is still an unconstrained factor.

Acknowledgments

This work was undertaken within the MAKs project funded by the German Ministry of Science and Education (BMBF). We thank the master and crew of the R/V Sonne for their support during the SO241 cruise. Further thanks goes to Regina Surberg, Bettina Domeyer, and Anke Bleyer for analytical support during the cruise and on shore. We greatly appreciate the support from Ana Kolevica, Tyler Goepfert, Sebastian Fessler, Andrea Bodenbinder, Yan Shen, and Jutta Heinze for onshore analyses. Additional support of this work was provided by EU-COST Action ES1301 "FLOWS" (www.flows-cost.eu).

References

- Aarnes, I., Svensen, H., Connolly, J. A. D. and Podladchikov, Y. Y.: How contact metamorphism can trigger global climate changes: Modeling gas generation around igneous sills in sedimentary basins, *Geochim. Cosmochim. Acta*, 74(24), 7179–7195, doi:10.1016/j.gca.2010.09.011, 2010.
- Aloisi, G., Drews, M., Wallmann, K. and Bohrmann, G.: Fluid expulsion from the Dvurechenskii mud volcano (Black Sea). Part I. Fluid sources and relevance to Li, B, Sr, I and dissolved inorganic nitrogen cycles, *Earth Planet. Sci. Lett.*, 225(3–4), 347–363, doi:10.1016/j.epsl.2004.07.006, 2004.
- Berndt, C., Hensen, C., Mortera-Gutierrez, C., Sarkar, S., Geilert, S., Schmidt, M., Liebetrau, V., Kipfer, R., Scholz, F., Doll, M., Muff, S., Karstens, J., Planke, S., Petersen, S., Böttner, C., Chi, W.-C., Moser, M.,

764 Behrendt, R., Fiskal, A., Lever, M. A., Su, C.-C., Deng, L., Brennwald, M. S. and Lizarralde, D.: Rifting
765 under steam – how rift magmatism triggers methane venting from sedimentary basins, *Geology*,
766 44(9), 767–770, 2016.

767 Biddle, J. F., Cardman, Z., Mendlovitz, H., Albert, D. B., Lloyd, K. G., Boetius, A. and Teske, A.:
768 Anaerobic oxidation of methane at different temperature regimes in Guaymas Basin hydrothermal
769 sediments, *ISME J.*, 6(5), 1018–1031, doi:10.1038/ismej.2011.164, 2012.

770 Blumenberg, M., Seifert, R., Reitner, J., Pape, T. and Michaelis, W.: Membrane lipid patterns typify
771 distinct anaerobic methanotrophic consortia, *Proc. Natl. Acad. Sci. USA*, 101, 11111–11116, 2004.

772 Brumsack, H. J. and Gieskes, J. M.: INTERSTITIAL WATER TRACE-METAL CHEMISTRY OF LAMINATED
773 SEDIMENTS FROM THE GULF OF CALIFORNIA, MEXICO, *Mar. Chem.*, 14, 89–106, 1983.

774 Calvert, S. E.: Accumulation of Diatomaceous Silica in the Sediments of the Gulf of California, *Geol.*
775 *Soc. Am. Bull.*, 77(June), 569–596, 1966.

776 Campbell, A. C. and Gieskes, J. M.: Water column anomalies associated with hydrothermal activity in
777 the Guaymas Basin, Gulf of California Andrew C. Campbell and Joris M. Gieskes, *Earth Planet. Sci.*
778 *Lett.*, 68, 57–72, 1984.

779 Chan, L. H., Gieskes, J. M., You, C. F. and Edmond, J. M.: Lithium Isotope Geochemistry of Sediments
780 and Hydrothermal Fluids of the Guaymas Basin, Gulf of California, *Geochim. Cosmochim. Acta*,
781 58(20), 4443–4454, 1994.

782 Curray, J. R. and Moore, D. G. et al.: Initial Reports of the Deep Sea Drilling Project. vol. 64., U.S.
783 Govt. Printing Office, Washington., 1982.

784 Von Damm, K. L., Edmond, J. M., Measures, C. I. and Grant, B.: Chemistry of submarine hydrothermal
785 solutions at Guaymas Basin, Gulf of California, *Geochim. Cosmochim. Acta*, 49(11), 2221–2237, 1985.

786 Von Damm, K.: Seafloor Hydrothermal Activity: Black Smoker Chemistry And Chimneys, *Annu. Rev.*
787 *Earth Planet. Sci.*, 18(1), 173–204, doi:10.1146/annurev.earth.18.1.173, 1990.

788 DeMaster, D.: The supply and accumulation of silica in the marine environment, *Geochim.*
789 *Cosmochimica Acta*, 5, 1715–1732, 1981.

790 Dickens, G. R.: Rethinking the global carbon cycle with a large, dynamic and microbially mediated gas
791 hydrate capacitor, *Earth Planet. Sci. Lett.*, 213(3–4), 169–183, doi:10.1016/S0012-821X(03)00325-X,
792 2003.

793 Dowell, F., Cardman, Z., Dasarathy, S., Kellermann, M. Y., Lipp, J. S., Ruff, S. E., Biddle, J. F., McKay, L.
794 J., MacGregor, B. J., Lloyd, K. G., Albert, D. B., Mendlovitz, H., Hinrichs, K. U. and Teske, A.: Microbial
795 communities in methane- and short chain alkane-rich hydrothermal sediments of Guaymas Basin,
796 *Front. Microbiol.*, 7(JAN), doi:10.3389/fmicb.2016.00017, 2016.

797 Einsele, G., Gieskes, J. M., Curray, J., Moore, D. M., Aguayo, E., Aubry, M.-P., Fornari, D., Guerrero, J.,
798 Kastner, M., Kelts, K., Lyle, M., Matoba, Y., Molina-Cruz, A., Niemitz, J., Rueda, J., Saunders, A.,
799 Schrader, H., Simoneit, B. and Vacquier, V.: Intrusion of basaltic sills into highly porous sediments,
800 and resulting hydrothermal activity, *Nature*, 283, 441–445, doi:10.1017/CBO9781107415324.004,
801 1980.

802 Fisher, A. T. and Becker, K.: Heat flow, hydrothermal circulation and basalt intrusions in the Guaymas
803 Basin, Gulf of California, *Earth Planet. Sci. Lett.*, 103(1–4), 84–99, doi:10.1016/0012-821X(91)90152-
804 8, 1991.

805 Gamo, T., Sakai, H., Kim, E.-S., Shitashima, K. and Ishibashi, J. -i.: High-alkalinity due to sulfate
806 reduction in the CLAM hydrothermal field, Okinawa Trough, Earth planet. Sci. Lett., 107, 328–338,
807 1991.

808 Gieskes, J. M., Kastner, M., Einsele, G., Kelts, K. and Niemitz, J.: Hydrothermal Activity in the Guaymas
809 Basin, Gulf of California: A synthesis, in In Initial Reports of the Deep Sea Drilling Project. vol. 64, Pt.
810 2, edited by D. G. et al. Curray, J.R., Moore, pp. 1159–1167., 1982.

811 Gieskes, J. M., Gamo, T. and Brumsack, H.: Chemical methods for interstitial water analysis aboard
812 Joides Resolution, Ocean Drill. Prog. Tech. Note 15. Texas A&M Univ. Coll. Stn., 1991.

813 Goldsmith, J. R., Graf, D. L. and Heard, H. C.: Lattice constants of the calcium-magnesium carbonates,
814 Am. Miner., 46, 453–457, 1961.

815 Grasshoff, K., Erhardt, M. and Kremling, K.: Methods of Seawater Analysis, Wiley-VCH, Weinheim.,
816 2002.

817 Gutjahr, M., Ridgwell, A., Sexton, P. F., Anagnostou, E., Pearson, P. N., Pälike, H., Norris, R. D.,
818 Thomas, E. and Foster, G. L.: Very large release of mostly volcanic carbon during the Palaeocene–
819 Eocene Thermal Maximum, Nature, 548(7669), 573–577, doi:10.1038/nature23646, 2017.

820 Hartmann, A. and Villinger, H.: Inversion of marine heat flow measurements by expansion of the
821 temperature decay function, Geophys. J. Int., 148(3), 628–636, doi:10.1046/j.1365-
822 246X.2002.01600.x, 2002.

823 Henry, P., Le Pichon, X., Lallement, S., Lance, S., Martin, J. B., Foucher, J. P., Fiala-Médioni, A., Rostek,
824 F., Guilhaumou, N., Pranal, V. and Castrec, M.: Fluid flow in and around a mud volcano seaward of
825 the Barbados accretionary wedge: Results from Manon cruise, J. Geophys. Res., 101(9), 20297–
826 20323, 1996.

827 Hensen, C., Nuzzo, M., Hornibrook, E., Pinheiro, L. M., Bock, B., Magalhães, V. H. and Brückmann, W.:
828 Sources of mud volcano fluids in the Gulf of Cadiz-indications for hydrothermal imprint, Geochim.
829 Cosmochim. Acta, 71(5), 1232–1248, doi:10.1016/j.gca.2006.11.022, 2007.

830 Howarth, R. J. and McArthur, J. M.: Strontium isotope stratigraphy, in A Geological Time Scale, with
831 Look-up Table Version 4, edited by F. M. Gradstein and J. G. Ogg, pp. 96–105, Cambridge University
832 Press, Cambridge, U.K pp. , 2004.

833 Huh, C.-A., Su, C.-C., Wang, C.-H., Lee, S.-Y. and Lin, I.-T.: Sedimentation in the Southern Okinawa
834 Trough – Rates, turbidites and a sediment budget, Mar. Geol., 231, 129–139, 2006.

835 Ivanenkov, V. N. and Lyakhin, Y. I.: Determination of total alkalinity in seawater, in In Methods of
836 Hydrochemical Investigations in the Ocean, edited by O. K. Bordovsky and V. N. Ivanenkov, p. 110–
837 114 (in Russian), Nauka Publishing House, Moscow., 1978.

838 Jahnke, R. A., Emerson, S. R. and Murray, J. W.: A model of oxygen reduction, denitrification, and
839 organic matter mineralization in marine sediments, Limnol. Oceanogr., 27(4), 610–623,
840 doi:10.4319/lo.1982.27.4.0610, 1982.

841 Jørgensen, B. B.: Bacteria and marine biogeochemistry, in Marine Geochemistry, edited by H. D.
842 Schulz and M. Zabel, pp. 169–206, Springer, Berlin., 2006.

843 Karaca, D., Hensen, C. and Wallmann, K.: Controls on authigenic carbonate precipitation at cold seeps
844 along the convergent margin off Costa Rica, Geochemistry, Geophys. Geosystems, 11(8), 1–19,
845 doi:10.1029/2010GC003062, 2010.

846 Kastner, M.: Evidence for Two Distinct Hydrothermal Systems in the Guaymas Basin, in *Initial*
847 *Reports of the Deep Sea Drilling Project*. vol. 64, Pt. 2, edited by D. G. et al. Curray, J.R., Moore, pp.
848 1143–1157, U.S. Govt. Printing Office, Washington., 1982.

849 Kastner, M. and Siever, R.: Siliceous Sediments of the Guaymas Basin: The Effect of High Thermal
850 Gradients on Diagenesis, *J. Geol.*, 91(6), 629–641, doi:10.1086/628816, 1983.

851 Kinoshita, M. and Yamano, M.: Hydrothermal regime and constraints on reservoir depth of the Jade
852 site in the Mid-Okinawa Trough inferred from heat flow measurements, *J. Geophys. Res.*, 102(B2),
853 3183–3194, 1997.

854 Koch, S., Berndt, C., Bialas, J., Haeckel, M., Crutchley, G., Papenberg, C., Klaeschen, D. and Greinert,
855 J.: Gas-controlled seafloor doming, *Geology*, 43(7), 571–574, doi:doi: 10.1130/G36596.1, 2015.

856 Lee, S.-Y., Huh, C.-A., Su, C.-C. and You, C.-F.: Sedimentation in the Southern Okinawa Trough:
857 enhanced particle scavenging and teleconnection between the Equatorial Pacific and western Pacific
858 margins, *Deep. Res.*, 51, 1769–1780, 2004.

859 Leefmann, T., Bauermeister, J., Kronz, A., Liebetrau, V., Reitner, J. and Thiel, V.: Miniaturized
860 biosignature analysis reveals implications for the formation of cold seep carbonates at Hydrate Ridge
861 (off Oregon, USA), *Biogeosciences*, 5, 731–738, 2008.

862 Lizarralde, D., Soule, S. A., Seewald, J. S. and Proskurowski, G.: Carbon release by off-axis magmatism
863 in a young sedimented spreading centre, *Nat. Geosci.*, 4(1), 50–54, doi:10.1038/ngeo1006, 2010.

864 Lonsdale, P. and Becker, K.: Hydrothermal plumes, hot springs, and conductive heat flow in the
865 Southern Trough of Guaymas Basin, *Earth Planet. Sci. Lett.*, 73(2–4), 211–225, doi:10.1016/0012-
866 821X(85)90070-6, 1985.

867 Lupton, J. E.: Helium-3 in the Guaymas Basin: Evidence for injection of mantle volatiles in the Gulf of
868 California, *J. Geophys. Res.*, 84(B13), 7446, doi:10.1029/JB084iB13p07446, 1979.

869 McDermott, J. M., Seewald, J. S., German, C. R. and Sylva, S. P.: Pathways for abiotic organic synthesis
870 at submarine hydrothermal fields, *PNAS*, 112(25), 7668–7672, 2015.

871 Milkov, A. V., Claypool, G. E., Lee, Y. J. and Sassen, R.: Gas hydrate systems at Hydrate Ridge offshore
872 Oregon inferred from molecular and isotopic properties of hydrate-bound and void gases, *Geochim.*
873 *Cosmochim. Acta*, 69(4), 1007–1026, doi:10.1016/j.gca.2004.08.021, 2005.

874 Nauhaus, K., Treude, T., Boetius, A. and Krüger, M.: Environmental regulation of the anaerobic
875 oxidation of methane: A comparison of ANME-I and ANME-II communities, *Environ. Microbiol.*, 7, 98–
876 106, 2005.

877 Niemann, H. and Elvert, M.: Diagnostic lipid biomarker and stable isotope signatures of microbial
878 communities mediating the anaerobic oxidation of methane with sulphate, *Org. Geochem.*, 39,
879 1668–1677, 2008.

880 Peckmann, J., Birgel, D. and Kiel, S.: Molecular fossils reveal fluid composition and flow intensity at a
881 Cretaceous seep, *Geology*, 37, 847–850, 2009.

882 Pfender, M. and Villinger, H.: Miniaturized data loggers for deep sea sediment temperature gradient
883 measurements, *Mar. Geol.*, 186(3–4), 557–570, doi:10.1016/S0025-3227(02)00213-X, 2002.

884 Schmidt, M., Hensen, C., Mörz, T., Müller, C., Grevemeyer, I., Wallmann, K., Mau, S. and Kaul, N.:
885 Methane hydrate accumulation in “Mound 11” mud volcano, Costa Rica forearc, *Mar. Geol.*, 216(1–
886 2), 83–100, doi:10.1016/j.margeo.2005.01.001, 2005.

887 Schmidt, M., Linke, P., Sommer, S., Esser, D. and Cherednichenko, S.: Natural CO₂ Seeps Offshore
888 Panarea : A Test Site for Subsea CO₂ Leak Detection Limit, *Mar. Technol. Soc. J.*, 49(1), 19–30, 2015.

889 Scholz, F., Hensen, C., Reitz, A., Romer, R. L., Liebetrau, V., Meixner, A., Weise, S. M. and Haeckel, M.:
890 Isotopic evidence (⁸⁷Sr/⁸⁶Sr, ^δ7Li) for alteration of the oceanic crust at deep-rooted mud volcanoes
891 in the Gulf of Cadiz, NE Atlantic Ocean, *Geochim. Cosmochim. Acta*, 73(18), 5444–5459,
892 doi:10.1016/j.gca.2009.06.004, 2009.

893 Scholz, F., Hensen, C., De Lange, G. J., Haeckel, M., Liebetrau, V., Meixner, A., Reitz, A. and Romer, R.
894 L.: Lithium isotope geochemistry of marine pore waters - Insights from cold seep fluids, *Geochim.*
895 *Cosmochim. Acta*, 74(12), 3459–3475, doi:10.1016/j.gca.2010.03.026, 2010.

896 Simoneit, B. R. T., Leif, R. N., Sturz, A. A., Sturdivant, A. E. and Gieskes, J. M.: Geochemistry of shallow
897 sediments in Guaymas Basin, gulf of California: hydrothermal gas and oil migration and effects of
898 mineralogy, *Org. Geochem.*, 18(6), 765–784, doi:10.1016/0146-6380(92)90046-Z, 1992.

899 Sommer, S., Linke, P., Pfannkuche, O., Schleicher, T., Deimling, J. S. V, Reitz, A., Haeckel, M., Flögel, S.
900 and Hensen, C.: Seabed methane emissions and the habitat of frenulate tubeworms on the Captain
901 Arutyunov mud volcano (Gulf of Cadiz), *Mar. Ecol. Prog. Ser.*, 382, 69–86, doi:10.3354/meps07956,
902 2009.

903 Śródoń, J.: Nature of Mixed-Layer Clays and Mechanisms of Their Formation and Alteration, *Annu.*
904 *Rev. Earth Planet. Sci.*, 27(1), 19–53, doi:10.1146/annurev.earth.27.1.19, 1999.

905 Svensen, H., Planke, S., Malthe-Sorensen, A., Jamtveit, B., Myklebust, R., Eidem, T. R. and Rey, S. S.:
906 Release of methane from a volcanic basin as a mechanism for initial Eocene global warming, *Nature*,
907 429(June), 3–6, doi:10.1038/nature02575.1., 2004.

908 Teske, A., Callaghan, A. V. and LaRowe, D. E.: Biosphere frontiers of subsurface life in the sedimented
909 hydrothermal system of Guaymas Basin, *Front. Microbiol.*, 5(JULY), 1–11,
910 doi:10.3389/fmicb.2014.00362, 2014.

911 Teske, A., De Beer, D., McKay, L. J., Tivey, M. K., Biddle, J. F., Hoer, D., Lloyd, K. G., Lever, M. A., Røy,
912 H., Albert, D. B., Mendlovitz, H. P. and MacGregor, B. J.: The Guaymas Basin hiking guide to
913 hydrothermal mounds, chimneys, and microbial mats: Complex seafloor expressions of subsurface
914 hydrothermal circulation, *Front. Microbiol.*, 7(FEB), 1–23, doi:10.3389/fmicb.2016.00075, 2016.

915 Timmers, P. H., Widjaja-Greefkes, H.A. Ramiro-Garcia, J., Plugge, C. M. and Stams, A. J.: Growth and
916 activity of ANME clades with different sulfate and sulfide concentrations in the presence of methane,
917 *Front. Microbiol.*, 6, 988, 2015.

918 Wallmann, K., Drews, M., Aloisi, G. and Bohrmann, G.: Methane discharge into the Black Sea and the
919 global ocean via fluid flow through submarine mud volcanoes, *Earth Planet. Sci. Lett.*, 248(1–2), 544–
920 559, doi:10.1016/j.epsl.2006.06.026, 2006.

921 Wegener, G., Krukenberg, V., Ruff, S. E., Kellermann, M. Y. and Knittel, K.: Metabolic capabilities of
922 microorganisms involved in and associated with the anaerobic oxidation of methane, *Front.*
923 *Microbiol.*, 7, 46, 2016.

924 Welhan, J. A.: Origins of methane in hydrothermal systems, *Chem. Geol.*, 71(1–3), 183–198,
925 doi:10.1016/0009-2541(88)90114-3, 1988.

926 Whiticar, M. J.: Carbon and hydrogen isotope systematics of bacterial formation and oxidation of
927 methane, , 161, 291–314, 1999.

928 Zachos, J. C., Wara, M. W., Bohaty, S., Delaney, M. L., Petrizzo, M. R., Brill, A., Bralower, T. J. and

929 Premoli-Silva, I.: A transient rise in tropical sea surface temperature during the Paleocene-Eocene
 930 thermal maximum., Science, 302(5650), 1551–1554, doi:10.1126/science.1090110, 2003.

931

932 Tables

933

934 Table 1: Station list and site names of GCs and MUCs taken in the Guaymas Basin with
 935 according water depth. Heat flow and temperature gradient data measured either attached
 936 to GCs or to a sediment probe.

Site	Site name	Latitude	Longitude	Water depth	Temp. gradient	Heat flow	SR	MAR
		(N)	(W)	(m)	(K m ⁻¹)	(mW m ⁻²)	(m kyr ⁻¹)	(g cm ⁻² yr ⁻¹)
GCs								
St.07-GC01	North Seep	27° 33.301'	111° 32.882'	1845	0.14	28	n.d.	n.d.
St.10-GC04	Reference Site	27° 26.531'	111° 29.928'	1846	0.22	140	n.d.	n.d.
St.09-GC03	Central Seep	27° 28.138'	111° 28.420'	1837	n.d.	n.d.	n.d.	n.d.
St.09-GC13	Central Seep	27° 28.193'	111° 28.365'	1838	0.16	113	n.d.	n.d.
St.72-GC15	Central Seep	27° 28.178'	111° 28.396'	1837	n.d.	n.d.	n.d.	n.d.
St.51-GC09	Smoker Site	27° 24.472'	111° 23.377'	1840	11	8069	n.d.	n.d.
St.58-GC10	Smoker Site	27° 24.478'	111° 23.377'	1845	10	6509	n.d.	n.d.
St.47-GC07	Slope Site	27° 24.412'	111° 13.649'	671	n.d.	n.d.	n.d.	n.d.
MUCs								
St.33-MUC11	North Seep	27° 33.301'	111° 32.883'	1855	n.d.	n.d.	1.7*	0.05*
							3.5 [#]	0.15 [#]
St.23-MUC05	Ring Seep	27° 30.282'	111° 40.770'	1726	n.d.	n.d.	0.5	0.01
St.15-MUC02	Reference Site	27° 26.925'	111° 29.926'	1845	n.d.	n.d.	2.3	0.04
St.22-MUC04	Central Seep	27° 28.165'	111° 28.347'	1839	n.d.	n.d.	1.7	0.04
St.65-MUC15	Smoker Site	27° 24.342'	111° 22.970'	1846	n.d.	n.d.	1.8	0.05
St.66-MUC16	Smoker Site	27° 24.577'	111° 23.265'	1842	n.d.	n.d.	2.1'	0.08'
							0.4 ⁺	0.02 ⁺
HF lance								
St.60a - HF008_P03	Smoker Site	27° 24.273'	111° 23.396'	1840	4.6	3206	n.a.	n.a.

St.60a - HF008_P01		27° 24.623'	111° 23.626'	1834	0.86	599	n.a.	n.a.
St.60a - HF008_P02		27° 24.554'	111° 23.512'	1840	2.8	1953	n.a.	n.a.
St.60a - HF008_P04		27° 24.408'	111° 23.288'	1849	2039	1427	n.a.	n.a.
St.60a - HF008_P05		27° 24.341'	111° 23.177'	1852	1014	710	n.a.	n.a.
St.60a - HF008_P06		27° 24.265'	111° 23.082'	1844	0.74	516	n.a.	n.a.
St.60b - HF008_P07		27° 24.193'	111° 23.956'	1834	0.8	579	n.a.	n.a.
St.60b - HF009_P04		27° 24.543'	111° 23.351'	1837	15	10835	n.a.	n.a.
St.60b - HF009_P01		27° 24.605'	111° 23.317'	1837	0.39	274	n.a.	n.a.
St.60b - HF009_P02		27° 24.552'	111° 23.347'	1834	3451	2415	n.a.	n.a.
St.70 - HF011_P01	Graben Site	27° 25.802'	111° 25.486'	1870	0.38	262	n.a.	n.a.
St.70 - HF011_P02		27° 25.460'	111° 24.946'	2019	0.48	338	n.a.	n.a.
St.70 - HF011_P03		27° 25.955'	111° 24.493'	2046	0.43	302	n.a.	n.a.
St.70 - HF011_P04		27° 25.837'	111° 24.951'	2025	0.46	320	n.a.	n.a.
Authigenic carbonate								
St.56-VgHG-4	Central Seep	27°28.181'	111°28.379'	1843	n.a.	n.a.	n.a.	n.a.

Abbreviations: SR, Sedimentation Rate; MAR, Mass Accumulation Rate; n.d., not determined; n.a., not applicable

*[#]Sedimentation and mass accumulation rates at Station 33 of the 0-13 cm, 13-18 cm layers, respectively

⁺Sedimentation and mass accumulation rates at Station 65 of the 0 - 7 cm, 7 - 17 cm layers, respectively

937

938

939

940

941

942

943

944

945

Figures

fig01

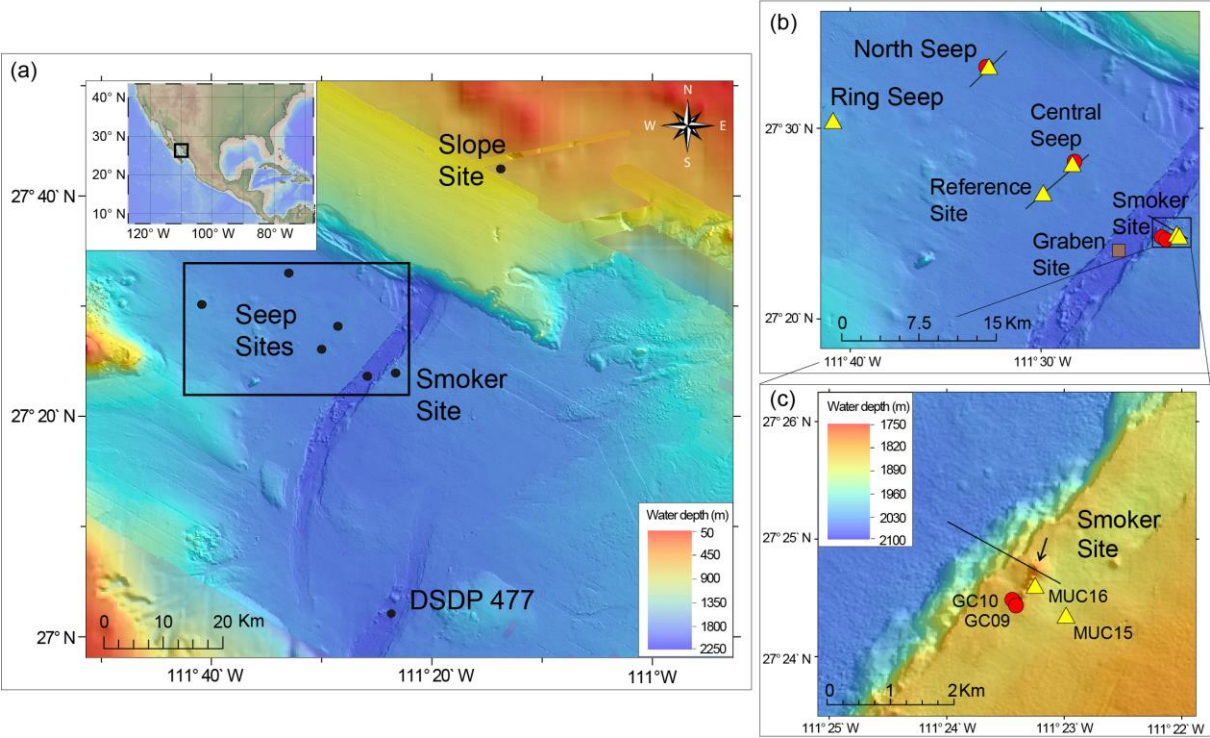
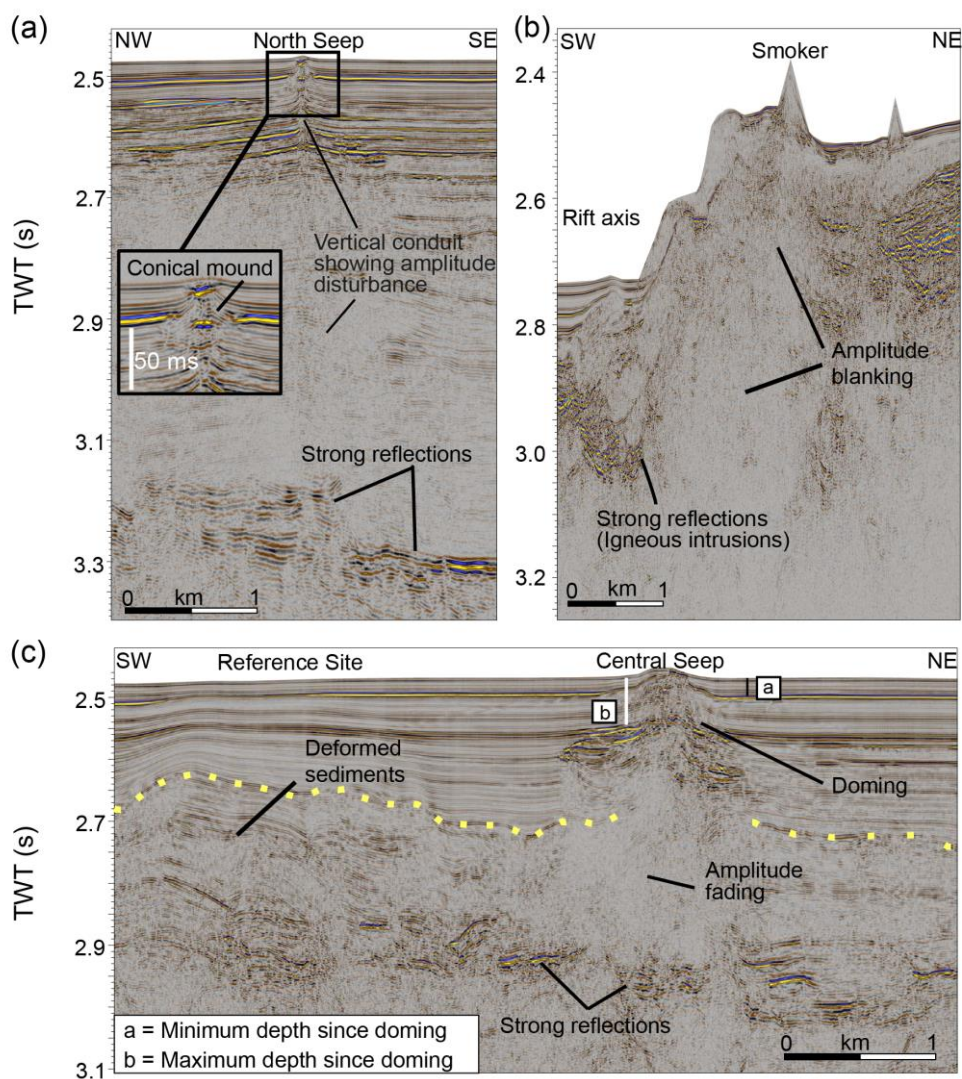


fig02



950

951

952

fig03

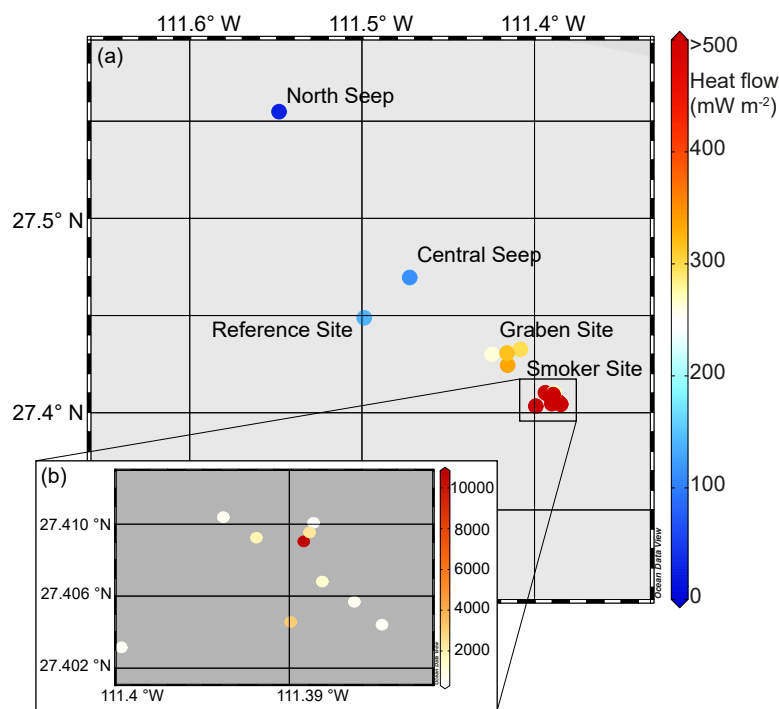


Fig04

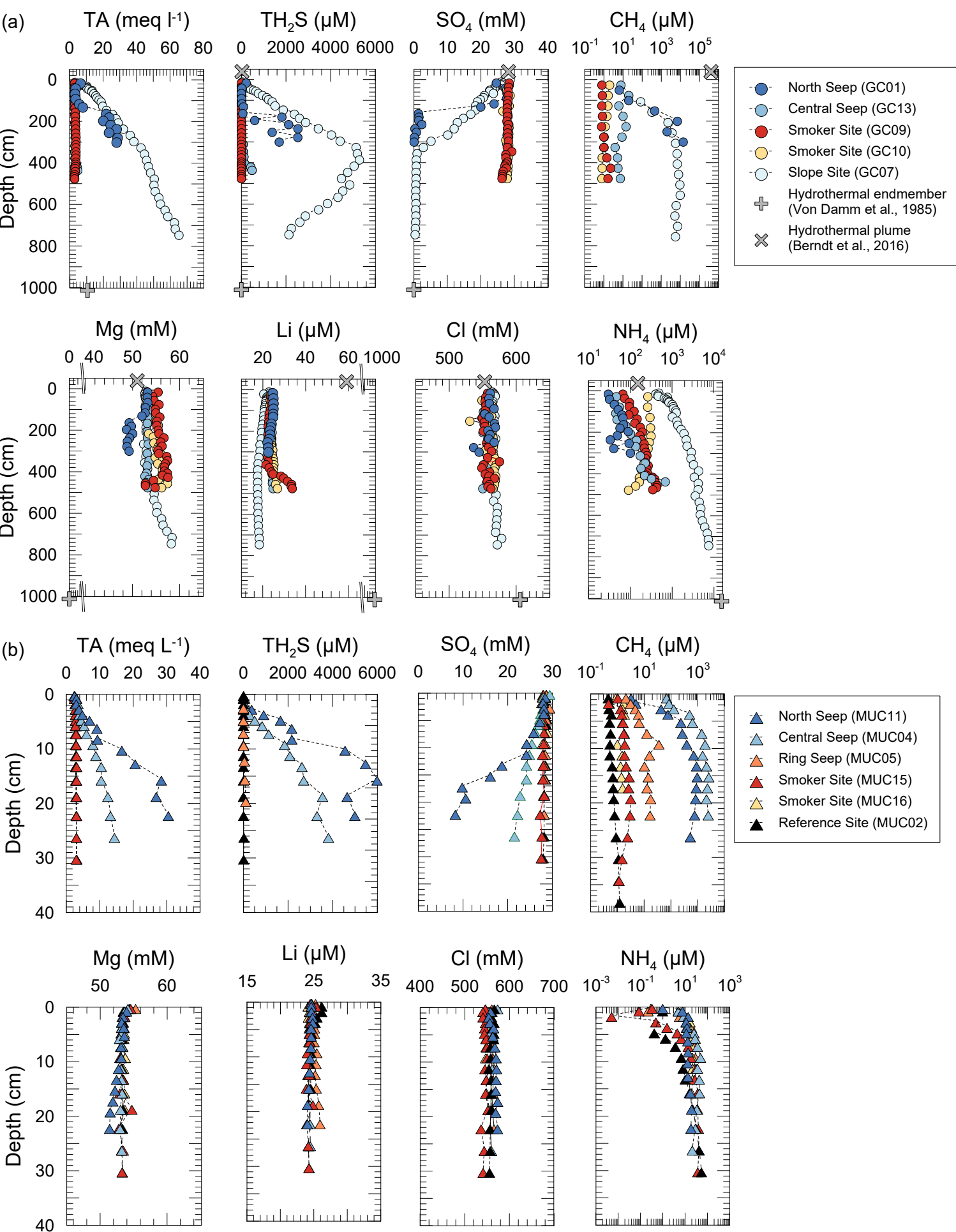


fig05

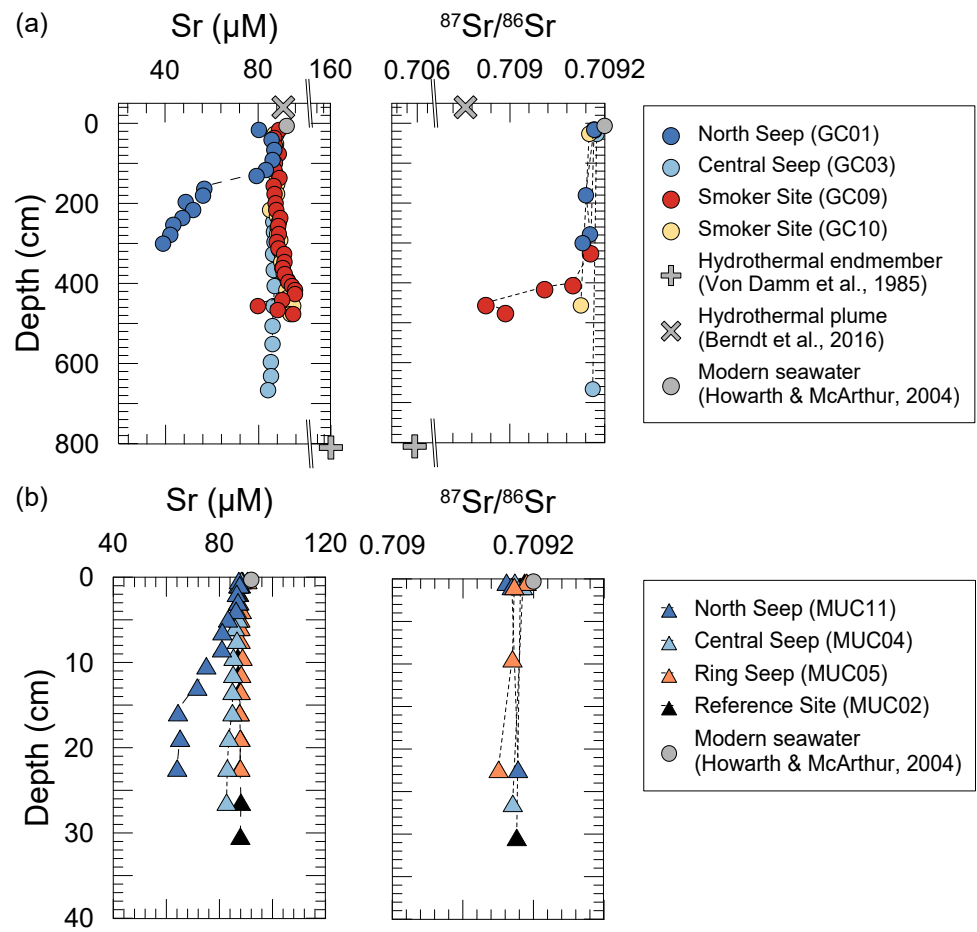


fig06

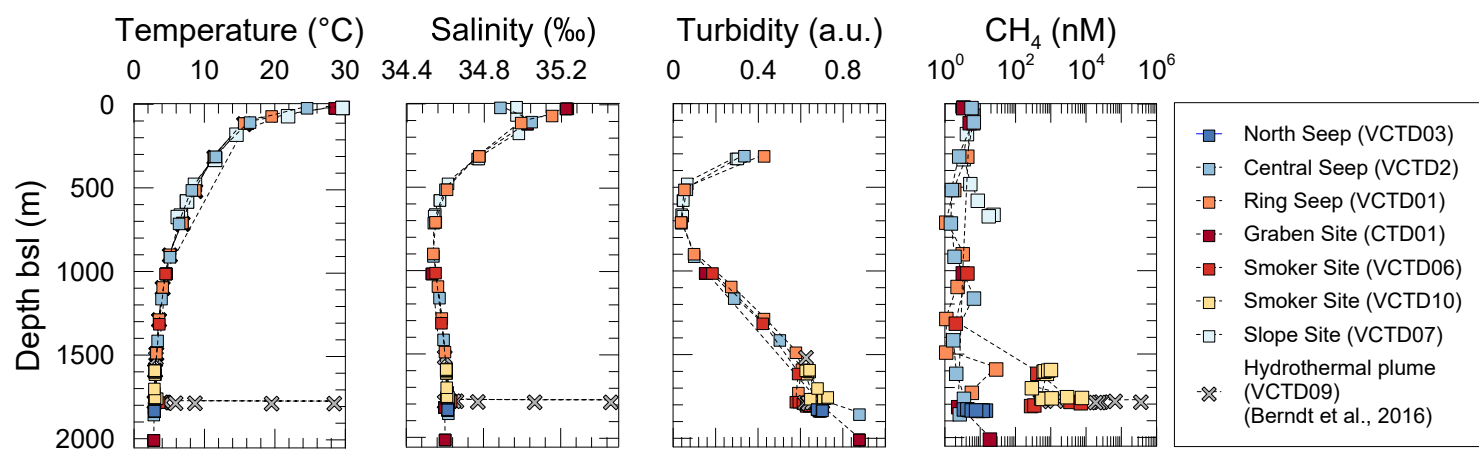
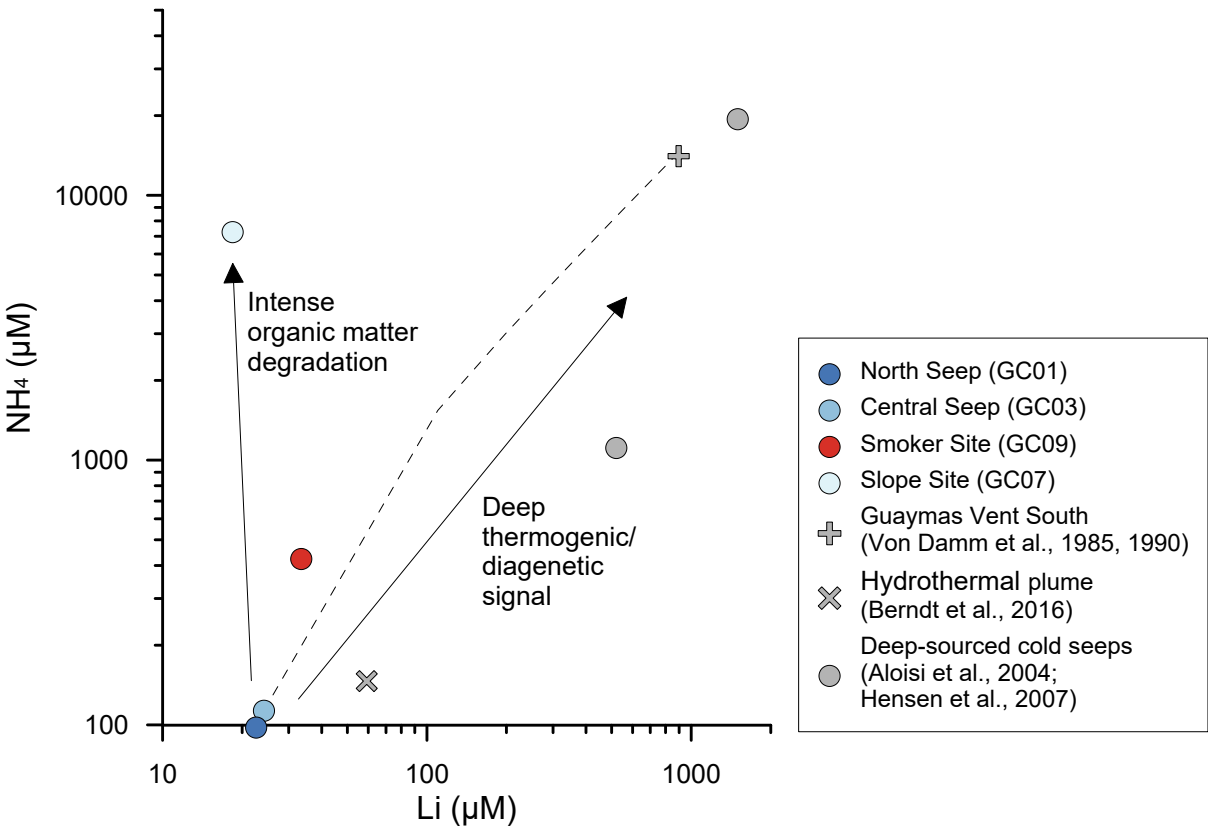


fig07



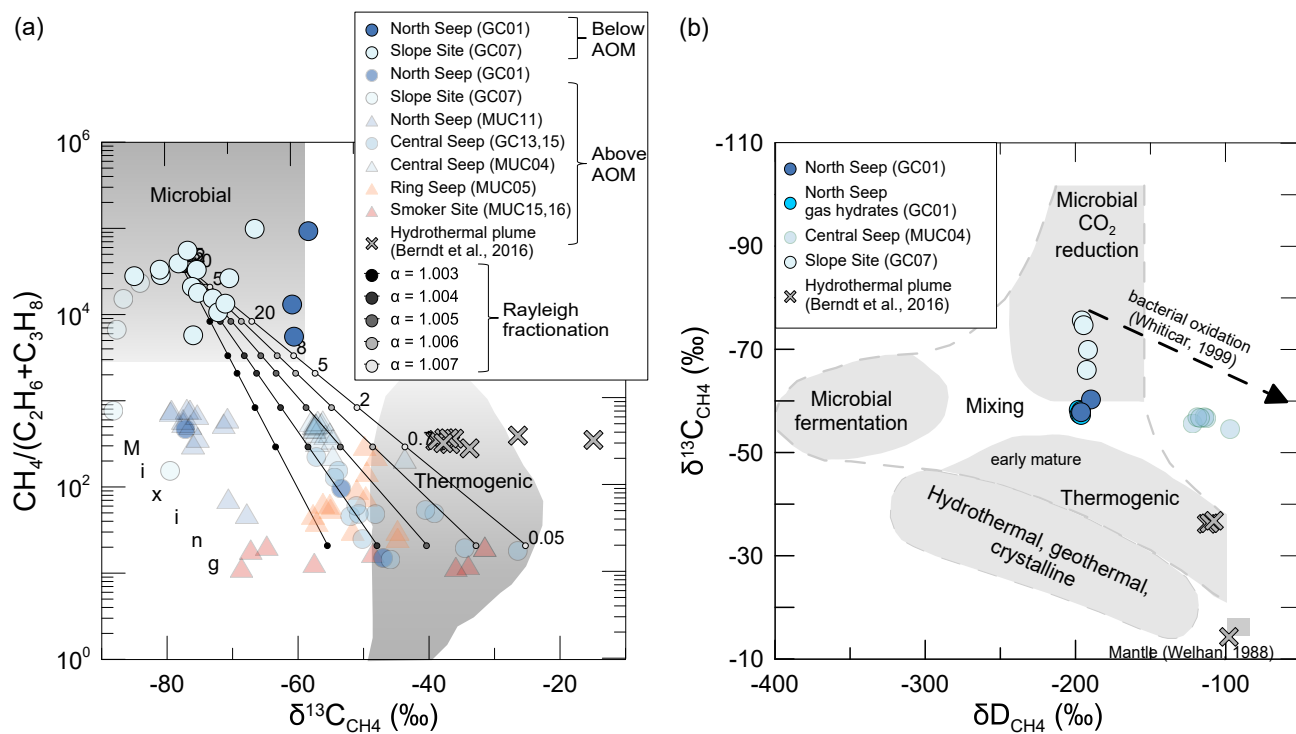


fig09

